Heterojunction In Situ Constructed by a Novel Amino Acid-Based Organic Spacer for Efficient and Stable Perovskite Solar Cells

Boxue Zhang, Deyu Gao, Mengjia Li, Xueni Shang, Ying Li, Cong Chen, Thierry Pauporté

Pease cite this paper as : B. Zhang, D. Gao, M. Li, X. Shang, Y. Li, C. Chen, Th. Pauporté, Heterojunction in-situ constructed by a novel amino acid-based organic spacer for efficient and stable perovskite solar cells. ACS Appl. Mater. Interfaces, 14 (2022) 40902–40912. DOI : 10.1021/acsami.2c09926

Heterojunction in-situ constructed by a novel amino acid-based organic spacer for efficient and stable perovskite solar cells

Boxue Zhang,[a,b] Deyu Gao,[a] Mengjia Li,[a] Xueni Shang,[a] Ying Li,[a] Cong Chen,[a,c]* Thierry Pauporté[b]*

[a]State Key Laboratory of Reliability and Intelligence of Electrical Equipment, School of Materials Science and Engineering, Hebei University of Technology, Tianjin 300401, China.

[b]Chimie ParisTech, PSL Research University, CNRS, Institut de Recherche de Chimie Paris (IRCP), UMR8247, 11 rue P. et M. Curie, F-75005 Paris, France.

[c]Macao Institute of Materials Science and Engineering (MIMSE), Macau University of Science and Technology, Taipa, Macau SAR, 999078 China.

*Corresponding authors. E-mail: chencong@hebut.edu.cn and thierry.pauporte@chimieparistech.psl.eu

Abstract

The optical properties and stability of metal halide perovskites can be improved by reducing their dimensionality. Since defects at the perovskite film grain body and boundaries cause significant energetic losses by non-radiative recombination, perovskite films with manageable crystal size and macroscopic grains are essential to improve the photovoltaic properties. Through theoretical calculation models and experiments, we show that the carboxyl group of 4-ammonium butyric acid-based cation (4-ABA$^+$) can interact with the three-dimensional (3D) perovskite to produce in-situ a secondary grain growth by post-treatment. It passivates the trap defects and broadens the light absorption. 4-ABA$^+$ could induce a 2D capping layer on top of 3D mixed cations-based perovskite to construct 2D /3D heterojunction. The 4-ABA$^+$ modified perovskite film consists of large-sized grains with extremely low trap state densities and possesses a longer charge carrier lifetime and good stability, resulting in efficient perovskite solar cells with a champion efficiency of 23.16% and a V_{OC} of 1.20 V. We show that the 4-ABA$^+$ treated devices outperform the 3-Ammonium Propionic Acid (3-APA$^+$) and 5-ammonium valeric acid (5-AVA$^+$) treated ones. Moreover, the devices exhibit high stability under high humidity and continuous light soaking conditions. This work gives a hint that our approach based on 4-ABA$^+$ treatment is key to achieve better electrical properties, a controlled crystal growth, as well as highly stable perovskite solar cells.

Keywords: 4-ammonium butyric acid; Hierarchical interface; 2D/3D Heterojunction; Defects passivation; Perovskite solar cell.

Pease cite this paper as : B. Zhang, D. Gao, M. Li, X. Shang, Y. Li, C. Chen, Th. Pauporté, Heterojunction in-situ constructed by a novel amino acid-based organic spacer for efficient and stable perovskite solar cells. ACS Appl. Mater. Interfaces, 14 (2022) 40902–40912. DOI : 10.1021/acsami.2c09926

1. Introduction

Organic-inorganic halide perovskites solar cells (PSCs) have received tremendous attention from scientists working on materials and devices during the last decade. Their present certified record power conversion efficiencies lie above 25%.[1-3] Although efficient PSCs have ignited the passion for photovoltaic research, the challenging issues which remain to be overcome are mainly recombination losses, band alignment, and stability since PSCs are sensitive to humidity, oxygen, and heat stressors.[2, 4-5] The instability of halide perovskites originates from their ionic nature and internal defects.[6-7] From the viewpoint of the crystal defects, three-dimensional (3D) perovskites are mainly prepared by solution-based technique, in which the crystallization processes include annealing and antisolvent promotion steps and will inevitably result in inferior crystal quality, excessive grain boundaries, and various forms of intrinsic defects.[8-9] The absence of comprehension of how intrinsic defects are formed and of strategies for eliminating them will inevitably limit the photovoltaic and stability performances.[10]

Structural engineering and interface engineering have been employed to eliminate intrinsic defects and enhance the stability of perovskites.[7,11] Structural engineering to build layered 2D perovskites of Ruddlesden–Popper type ($Y_2A_{n-1}B_nX_{3n+1}$) and Dion–Jacobson type ($YA_{n-1}B_nX_{3n+1}$) show higher environmental stability because of the hydrophobicity of large size organic cations with long alkyl chains while it inevitably sacrifices the photovoltaic performance of the PSCs.[12] Interface engineering by depositing a hydrophobic organic cation (such as Butylammonium (BA^+), phenethylammonium (PEA^+),[13] and 5-ammonium valeric acid (5-AVA^+)) on top of the 3D perovskite surface to coordinate the dangling bonds of 3D perovskite and form 3D/2D interfacial heterojunctions has been regarded as an effective way to mitigate the non-radiative recombination, minimize the density of defects and regulate the stability.[14] Cations are mainly deposited or incorporated to form low-dimensional layers through strong hydrogen bond linkage and achieve enhanced cross-linking effects, leading to reduced defect density and improved interfacial charge extraction efficiency. To efficiently modify the perovskites, organic ammonium ions are introduced to occupy octahedral sites (PbI_6^{4-}) on the top side of crystals and not into their lattice. The potential benefits of this method are fourfold. (i) First, during the film deposition process, the cations existing at the interface can improve the chemical linking ability between the absorber layer and the hole transporting layer through the functional groups. (ii) These cations can be used for the growth control or guidance factors and facilitate the formation of uniform thin films with dense morphology. (iii) Cations can passivate high-density defects on the surface, which usually act as an origin of “pitting” to cause the decomposition of perovskite. (iv) Large-sized cations can form low-dimensional structures on the top side, making absorber thin films unaffected by moisture and then more stable in the long run.

The photovoltaic properties of the resultant low-dimensional perovskites are greatly affected by the chemistry of the additive molecules, which then offer great potential for the preparation of perovskite materials with customized characteristics. Among the above-mentioned large cations, 5-AVA^+ has been employed as an excellent dopant to tailor the crystal structure of the absorber layer, resulting in an improved charge carrier lifetime.[15] For example, Mei et al. showed that the $MAPbI_3$ crystals were strengthened by 5-AVA^+ at the grain boundaries and they indicated that the decomposition and ionic migration could be inhibited, meeting stability standards of IEC61215:2016

qualification tests during 9000 h.[16] However, 5-AVA$^+$ based cationic additives studied so far are mainly incorporated into the adjacent perovskite crystal in a low-dimensional form. Moreover, the long alkyl chain (four alkyl groups inside) is still the bottleneck limiting the electrical properties of 5-AVA$^+$ doped low-dimensional perovskite.[13] Introducing large-sized cations with an alkyl chain will inevitably inhibit the longitudinal transport of carriers while improving the stability of the perovskite. Similar to 5-AVA$^+$, 4-ABA$^+$ is an amino acid with three alkyl groups inside, one carboxyl group, and one amino functional group. The shorter alkyl chain length will benefit the charge transfer between layers in the produced low-dimensional perovskite.

In this work, we develop a new organic amino-acid cation, 4-ABA$^+$, as an interfacial ionic solution to obtain a 2D capping layer on top of 3D mixed cations-based perovskite to construct 2D /3D heterojunction. Our results demonstrate the following multiple benefits: (i) 4-ABA$^+$ can form a low-dimensional capping layer with higher surface potential for effectively regulating the bandgap alignment and reducing V_{OC} loss; (ii) Hydrogen bonds can be formed between COOH and NH_3^+ groups of 4-ABA$^+$ and I^- ions from PbI_6^{4-} octahedra; (iii) −COOH in 4-ABA$^+$ can act as a suitable hydrogen donor/acceptor with hydrogen bonding to each other,[17] giving a hierarchical interface to reduce the density of defect states. (iv) 4-ABA$^+$ enhance the perovskite recrystallization. It results in increased grain size by the dehydration-condensation reaction of amino acids. This strategy combines the advantages of defect passivation and water repellency by the low dimensional perovskite interfacial layer.

2. Results and discussion

The perovskite photoactive layer was prepared on SnO_2 by a typical one-step spin-coating technique and was annealed on a hotplate at 110°C. The rapid crystallization of 3D perovskite crystals usually results in small-sized grains with a high density of traps. The perovskite layer was subsequently treated by spin-coating a solution of 4-ABAI dissolved in isopropyl alcohol (IPA) solvent and annealed at 110 ºC to fabricate a 4-ABA$^+$ based low-dimensional perovskite capping layer (**Figure 1a**). Similar to the popular 5-AVA$^+$, 4-ABA$^+$ contains a carbonyl group, an amino group, and a chain of four alkyl groups. **Figure 1b** provides the working mechanism of 4-ABA$^+$ in the perovskite. Specifically, the carbonyl group can combine with under-coordinated Pb^{2+} ions or trap states with a positive charge to form Lewis adducts and passivate defects at the crystal grains or surface. As a novel organic amine cation, 4-ABA$^+$ could help to form quasi-2D perovskite through the cations exchange process and in-situ reaction with PbI_2. We implemented SEM top-view imaging of the control and 4-ABA$^+$ modified perovskite films. Usually, there are some bright PbI_2 crystals on top of the control perovskite films (**Figure 1c**).[18] Introducing 4-ABA$^+$ markedly changed the surface morphology (**Figure 1d**) by *in-situ* formation of 2D $(4\text{-ABA})_2A_{n-1}Pb_nX_{3n+1}$ perovskite on the surface. The 4-ABA$^+$ long-chain molecules can effectively recrystallize the perovskite.[19] Furthermore, due to the dehydration condensation reaction of amino acid molecules, multiple 4-ABA$^+$ ions will produce long-chain amino acids through a chemical reaction and then produce H_2O. These water molecules will further promote the growth of perovskite grains for the PbI_2 crystals recrystallization through an Oswald ripening effect.[20] By using the AFM height sensor mode **(Figure 1e-f)**, we measured root means square (RMS) values of 25.4 nm and 16.6 nm for the control and 4-ABA$^+$ modified perovskite films, respectively, demonstrating the

surface flattening. The 3D perovskite changed from a rough surface with small crystal grains to a flat, uniform, and dense morphology after the 4-ABA^+ treatment. In **Figure S1** (Supporting information), the average grain size gradually grows with the concentration of 4-ABA^+ from 1 to 3 mg/mL. The increased grain size may be assigned to the dehydration-condensation reaction of amino acids in 4-ABA^+, which promotes the recrystallization process of perovskite. However, as the concentration reached 5 mg/mL, the film surface was covered with excessive 4-ABA^+ or $(4\text{-ABA})_2X_{n-1}Pb_nI_{3n+1}$ film, producing a decreased interfacial carrier transporting characteristics because of the lower conductivity of 2D perovskite. The optimized 2D capping layer eliminated the superficial defects and reduced the loss of interfacial charge by recombination. It also induced a second crystal growth of perovskite, which appears as a crucial factor in getting high-efficiency devices.

X-ray photoelectron spectroscopy (XPS) measurements were carried out on control and 4-ABA^+-modified perovskite films to determine the chemical compositions (**Figure 1g-h and Figure S2**, Supporting information). As expected, the C1s peak exhibits contributions from atmospheric CO_2, 4-ABA^+ (containing a carboxyl, amide, and alkyl group), and A-site perovskite organic component (FA^+, MA^+). The active binding of 4-ABA^+ was first confirmed by the appearance in the C1s spectra of the modified perovskite film of C=O, C-C, O=C-O, and C-OH bond signals. The O 1s peaks from XPS spectra are related to the 2D component, relating to the -C=O from carboxyl contained in 4-ABA^+. Furthermore, the XPS spectra of N 1s, Pb 4f, Br 3d, I 3d, and Cs 3d show that the passivation layer did not alter the original structure of the control perovskite films. Fourier transforms infrared spectroscopy (FTIR) in **Figure S3** (Supporting Information) shows that the C=O vibration peak at about 1700 cm^{-1} has shifted to a higher wavenumber, proving the strong interaction between the control and 4-ABA^+ modified perovskite films. XRD analysis of the perovskite films and the prepared 2D perovskite references with various n values (n=1, 2, 3, 4) are reported in **Figure 1i** and **Figure S4** (Supporting information), respectively. The control film shows a clear peak at 12.7°, indicating the presence of excess and unreacted PbI_2 in the as-prepared control perovskite films. After introducing 3 mg/mL 4-ABA^+ with an annealing temperature of 100°C, we observed the decreased PbI_2 diffraction peak intensity, revealing that 4-ABA^+ could react with PbI_2 to form the low-dimensional perovskite. Furthermore, a characteristic peak at 6° in the 4-ABA^+ modified perovskite film proves the presence of 2D components (**Figure 1i**).[21-23]

The UV-Vis absorption spectra in **Figure S5** reveal that the 4-ABAI modification unchanges the light absorbance of the perovskite layer and produces a slight redshift, which slightly expands the absorber light-harvesting capacity. As we discussed earlier, 4-ABA^+ is a multifunctional ion due to its exposed carboxyl and amino functional groups. In order to prove that 4-ABA^+ has advantages over traditional BA^+ (BA^+ stands for butylamonium) and $5AVA^+$ cations. We proved the carboxyl–iodine interaction in $(4\text{-ABA})_2(MA)_{n-1}Pb_nI_{3n+1}$ perovskites with n=2 cases by comparing $(4\text{-ABA})_2MAPb_2I_7$ with $(BA)_2MAPb_2I_7$, and $(5\text{-AVA})_2MAPb_2I_7$ compounds modelled by DFT-based calculations (**Figure S6a-c**, **Table S1,** Supporting information). For $(4\text{-ABA})_2MAPb_2I_7$, we observed a significant tendency for two -COOH atoms of 4-ABA^+ to aggregate, unlike the case of $(BA)_2MAPb_2I_7$, where the $-CH_2-$ chain remains almost upright. The closest distance between the -COOH atoms of two 4-ABA^+ is about 3 Å. It is a reasonable distance for a carboxyl-carboxyl interaction. Besides, $(5AVA)_2MAPb_2I_7$ is similar in structure to $(4\text{-ABA})_2MAPb_2I_7$, but it has a longer alkyl chain, which deforms the perovskite.

Pease cite this paper as : B. Zhang, D. Gao, M. Li, X. Shang, Y. Li, C. Chen, Th. Pauporté, Heterojunction in-situ constructed by a novel amino acid-based organic spacer for efficient and stable perovskite solar cells. ACS Appl. Mater. Interfaces, 14 (2022) 40902–40912. DOI : 10.1021/acsami.2c09926

The carboxyl-carboxyl interaction can make the structure more stable, thereby enhancing the stability of the perovskite. The electronic band structure (**Figure S6d-f**) shows the conduction band edge and valence band edge of 2D perovskite. Compared to $(BA)_2MAPb_2I_7$ and $(5\text{-}AVA)_2MAPb_2I_7$, the valence band edge of $(4\text{-}ABA)_2MAPb_2I_7$ is close to the conduction band edge. The tDOS indicates that the energy of the valence band edge is mainly due to the iodine contribution. The strong interaction of the $4\text{-}ABA^+$ molecule with the I^- ion changes the band structure of the perovskite, thereby narrowing the bandgap and improving light absorption (**Figure S6g-i**, Supporting information).

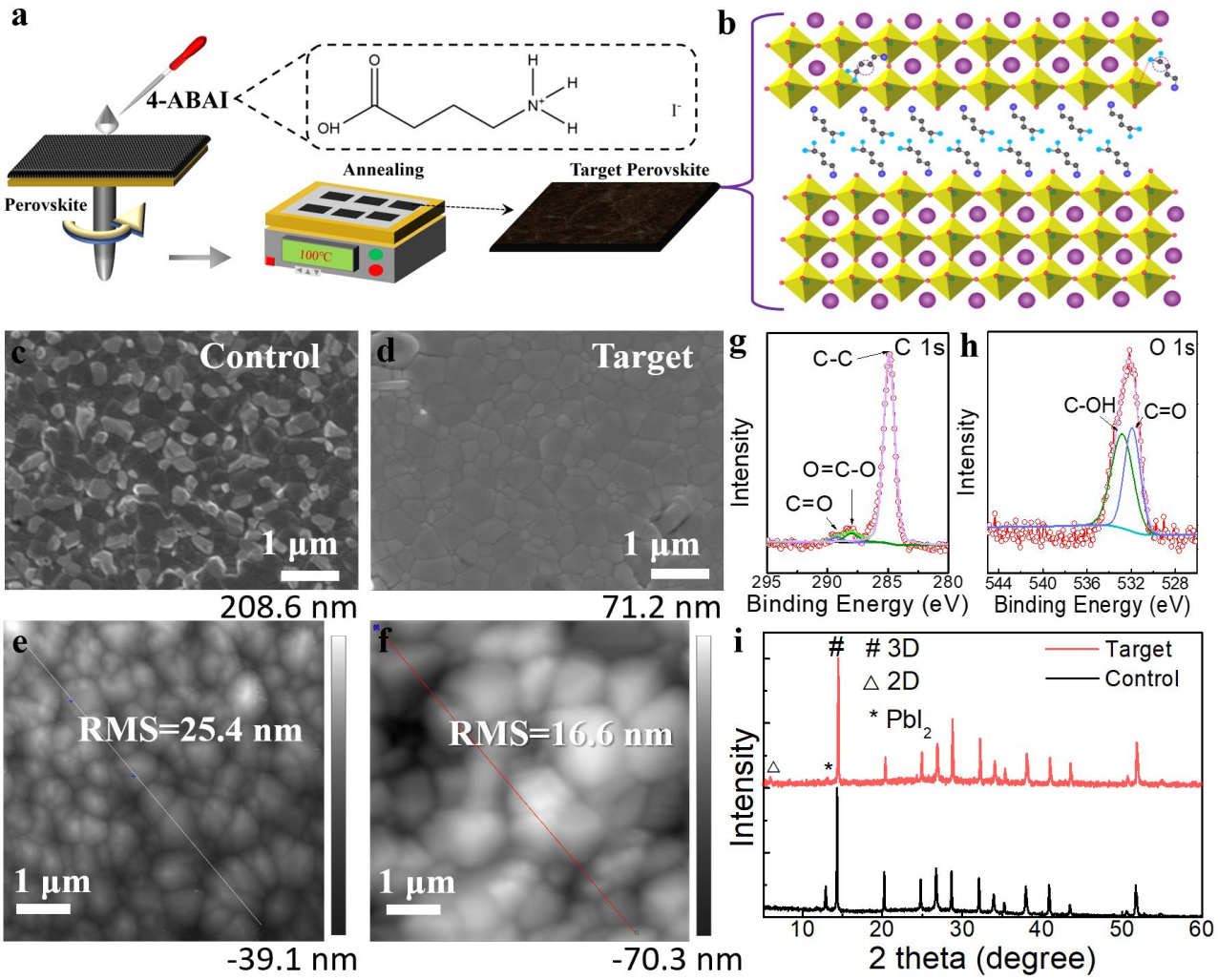

Figure 1. (a) Scheme of the perovskite film treatment process. Inset is the chemical structure of 4-ABAI. (b) Schematic crystal structure of $4\text{-}ABA^+$ modified perovskite to construct 2D/3D heterojunction. SEM top-view images of the (c) control and (d) 3 mg/mL $4\text{-}ABA^+$ modified $Cs_{0.05}(FA_{0.83}MA_{0.17})_{0.95}PbI_{0.83}Br_{0.17}$ perovskite film. XPS spectra of 2D/3D perovskite films for (g) C 1s and (h) O 1s detection. AFM height sensor image of the (e) control and the (f) $4\text{-}ABA^+$ modified perovskite films, (i) XRD patterns of the control and 3 mg/mL $4\text{-}ABA^+$ modified perovskite films.

We then prepared PSCs with the device structure of FTO/SnO_2/perovskite/Spiro-OMeTAD/Au (**Figure 2a and b**). It can be seen from the cross-section SEM image that the $4\text{-}ABA^+$ modified perovskite film has flatter and long-range ordered grains, while the traditional film has many small grains, which is consistent with the surface SEM analysis. At the same time, the functional layer

including glass /FTO, SnO_2, perovskite, spiro-OMeTAD, and Au counter electrode of the whole device are evenly distributed, which is the basis of high-efficiency devices. To prove the universality of 4-ABA^+ modification on the photovoltaic performance, we simultaneously prepared two kinds of PSCs containing a typical mixed three cations CsFAMA precursor system ($Cs_{0.05}(FA_{0.83}MA_{0.17})_{0.95}PbI_{0.83}Br_{0.17}$) and a double-cations CsFA precursor system with MACl as an additive. The photovoltaic characteristics of these devices are analyzed in detail. A statistical distribution diagram of the PCEs as a function of the 4-ABA^+ concentration is reported in **Figure 2c** and **Figure S7** (Supporting Information). The statistical graph from 25 individual PSC devices reveals that the 3 mg/mL 4-ABA^+ modification could help to achieve a better reproducibility.

As for the CsFA precursor system-based high-efficiency device, the control PSCs could exhibit a best PCE of 19.86%, while the PCE value increased to 20.96%, 21.93%, and 23.16% for 1 mg/mL, 2 mg/mL, and 3 mg/mL 4-ABA^+ modified PSCs. It dropped to 22.15%, and 20.72% as the concentration reached 4 mg/mL and 5 mg/mL, respectively.[24] As is illustrated from the champion photovoltaic performance in **Figure 2d** from the typical current density-voltage (*J-V*) results, the CsFA precursor system based PSC device increased from 19.86% (Voc=1.12 V, Jsc=23.37 mA/cm^2, FF =75.87%) to 23.16% (Voc=1.20 V, Jsc =24.57 mA/cm^2, FF=78.55%). The integral photocurrents from the EQE response (**Figure S8**, Supporting information) exceeding 800 nm of the CsFA precursor system-based control and 4-ABA^+ modified PSCs are 24.37 mA/cm^2 and 23.00 mA/cm^2, respectively. The integral photocurrents are consistent with the current density-voltage (*J-V*) results (**Figure 2d**). The best cell photovoltaic parameters with and without treatment are gathered in **Table 1**. In particular, the V_{OC} was improved from 1.12 V to 1.20 V, which can be associated with the improved interfacial contact and crystal quality. As extensively reported in the literature on PSC devices, *J-V* curves of the control PSCs present strong hysteresis behavior. The hysteresis can be related to the electrical bias-induced instability at the perovskite/spiro-OMeTAD interface, linked to the electrochemical reactivity of the perovskite layer. In our case, the 4-ABA^+ based low-dimensional capping layer can effectively passivate the A-site vacancy on the surface of 3D perovskite, improve the energy band structure of the interface, inhibit the halide ion migration at the same time,[25] and thus reduce the hysteresis effect of devices. **Figure S9** show the stabilized J_{SC} and PCE for the control and 4-ABA^+ modified CsFA precursor system-based PSCs tested at the maximum power point (MPP) with a bias voltage of 0.94 V and 1.02 V, respectively. After continuous illumination for 300 s, the control and modified CsFA precursor system-based device held a steady-state J_{SC} of 20.87 mA·cm^{-2}, and 22.49 mA·cm^{-2}, respectively, resulting in the steady-state PCE of 22.93% and 19.61%. Simultaneously, the modified device exhibited a lower leakage current from the dark current densities (**Figure S10,** Supporting information).

In the meantime, we also found that the control and 3 mg/mL 4-ABA^+ modified traditional $Cs_{0.05}(FA_{0.83}MA_{0.17})_{0.95}PbI_{0.83}Br_{0.17}$ based PSCs could achieved photovoltaic performance of 19.52% (Voc=1.08 V, Jsc=23.44 mA/cm^2, FF=77.10%) and 22.25% (Voc=1.14 V, Jsc=23.85 mA·cm^{-2}, FF=81.83%), as shown in **Figure S11** (Supporting Information). This indicates that 4-ABA^+ is an universal post-treatment agent for low dimensional modification and photovoltaic performance improvement of PSCs, and it is independent of the components of perovskite materials. We further tested the photovoltaic performance of the 3-Ammonium Propionic Acid (3-APA^+) and 5-AVA^+

modified $Cs_{0.05}(FA_{0.83}MA_{0.17})_{0.95}PbI_{0.83}Br_{0.17}$ based devices and achieved efficiencies of 22.12% and 21.01%, respectively (**Figure S12**). The comparison indicates that 4-ABA^+ as a space modifier has better photovoltaic performance than 3-APA^+ and 5-AVA^+. Although 4-ABA^+ and 5-AVA^+ exhibit the same terminal functional groups (carbonyl and amino), 4-ABA^+ has less alkyl chain length than 5-AVA^+. As an organic spacer cation for low-dimensional modification, a shorter alkyl chain length is conducive to charge carrier transfer between inorganic $[PbI_6]^{4-}$ layers, thus promoting the improvement of photovoltaic performance of devices.

In the above, we attributed the effect of 4-ABA^+ on the increased grain size and device performance to the following aspects: (1) As an amino acid molecule, 4-ABAI can produce water molecules by dehydration condensation reaction between multiple 4-ABAI molecules during annealing after spin coating on the perovskite surface. The existence of water molecules promotes the secondary crystallization of perovskite films and then promotes the secondary growth of grains. This is a typical Oswald ripening effect caused by the presence of water molecules; (2) As an organic ammonium salt, 4-ABA^+ can effectively hinder the charge recombination at the perovskite crystal surface, which is similar to PEA^+, PA^+, BA^+, 5-AVA^+ and $THMA^+$ in previous studies[16, 26]. Large organic ammonium salts as a spacer can be inserted into the surface of 3D perovskite to form a 2D/3D layered structure (although it is not necessarily a pure 2D structure, it may be an $A_2B_{n-1}M_nX_{3n+1}$ with high n-value). The recrystallized 2D perovskite on the surface of 3D perovskite will passivate the A-site cation vacancy. 4-ABA^+ constructed low dimensional perovskite also inhibits the interfacial charge recombination between perovskite/hole transport layers. (3) The excess or unreacted PbI_2 on the perovskite surface will react directly with 4-ABA^+, which can be seen from the significantly decreased XRD diffraction peak of PbI_2. It shows that 4-ABA^+, as a new organic ammonium salt, will definitely and inevitably in situ generate new low-dimensional perovskite on the surface.

The plot of the solar cell V_{OC} versus the light intensity provided detailed information about recombination processes occurring in devices due to trap states **(Figure 2e)**. It can be modelled using the following formula:

$$V_{OC} = n\left(\frac{K_B T}{e}\right) ln(I) + constant \qquad (1)$$

where n is the ideality coefficient, K_B is the Boltzmann constant, e is the elemental charge, T the absolute temperature, and I the intensity of light. The 4-ABA^+ modified PSCs exhibited a lower slope (n=1.26) compared to the control device (n=1.45), indicating the effectively weakened trap-induced carrier recombination. The impedance spectra (**Figure 2f**). were measured in the dark to clarify the charge transfer and recombination processes in the PSCs.[3] The modified device exhibited a R_{rec} value of 1036 Ω, a value higher than 724 Ω measured for the control device, proving the effective suppression of recombination rate. The above electrical properties fully illustrate the reduced trap states for carrier recombination after introducing 4-ABA^+, which is beneficial for high charge extraction efficiency.

Pease cite this paper as : B. Zhang, D. Gao, M. Li, X. Shang, Y. Li, C. Chen, Th. Pauporté, Heterojunction in-situ constructed by a novel amino acid-based organic spacer for efficient and stable perovskite solar cells. ACS Appl. Mater. Interfaces, 14 (2022) 40902–40912. DOI : 10.1021/acsami.2c09926

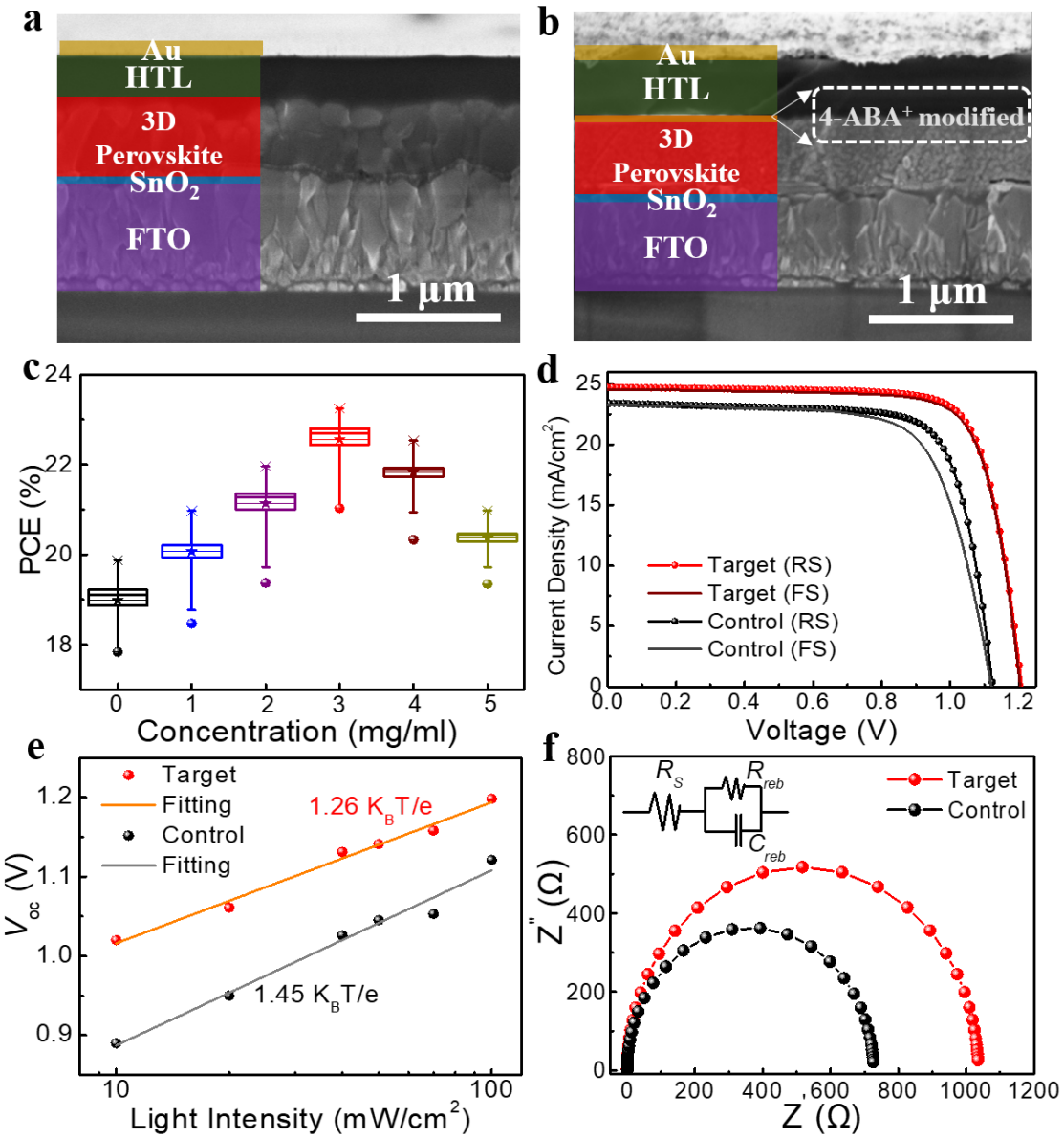

Figure 2. Cross-sectional SEM image of the full (a) control and (b) 4-ABA$^+$ modified $Cs_{0.05}(FA_{0.83}MA_{0.17})_{0.95}PbI_{0.83}Br_{0.17}$ based PSC devices. (c) PCE distribution of the PSCs with different concentrations of 4-ABA$^+$ from 0 mg/mL to 5 mg/mL. (d) Typical *J-V* curves of best champion devices with and without 4-ABA$^+$. The *J-V* curve of the highest-efficiency device is obtained from the CsFA precursor system. (e) Seminatural-logarithmic plots of V_{OC} versus light intensity. (f) Nyquist plots at 0 V (1 Hz to 100 kHz) of the control and 4-ABA$^+$ modified PSC device.

Samples	Scanning direction	V_{OC}(V)	J_{SC} (mA·cm^{-2})	*FF*(%)	*PCE*(%)
Control	RS	1.12	23.37	75.87	19.86
	FS	1.11	23.32	70.65	18.29
With 4-ABA$^+$	RS	1.19	24.63	77.89	22.83

Pease cite this paper as : B. Zhang, D. Gao, M. Li, X. Shang, Y. Li, C. Chen, Th. Pauporté, Heterojunction in-situ constructed by a novel amino acid-based organic spacer for efficient and stable perovskite solar cells. ACS Appl. Mater. Interfaces, 14 (2022) 40902–40912. DOI : 10.1021/acsami.2c09926

	FS	1.20	24.57	78.55	23.16

Table 1 Photovoltaic characteristics of best CsFA devices prepared without and with 4-ABA$^+$ treatment at forward (FS) and reverse (RS) scans.

Kelvin probe force microscopy (KPFM) was employed to provide a reliable measure of the local surface potential that originates from contact potential differences (CPD) mappings (**Figure 3a** and **b**) between the microscope tip and the sample surface. The measure provides their relative work functions, the V_{OC} promotion, and the possibility of bandgap bending along grain boundaries.[27] 4-ABA$^+$ modification affected the mean values (**Figure 3c**) of the CPD in the perovskite film, which increased from 213~282 mV to 521~646 mV due to the abundant electron density over the outer contour of 4-ABA$^+$. Given that the work function of the metal tip is higher than the perovskite surface, higher CPD corresponds to a larger work function difference between the tip and samples. The higher surface potential shift indicates a better energy band alignment. It may favour electron extraction and hole transportation. The larger CPD points out a higher Fermi energy level which enlarges the build-in potential. It agrees with the improved V_{OC} for 4-ABA$^+$ modified PSCs. Another insight is the higher CPD within the interior of the grain boundaries. The properties of grain boundaries and variations in electronic properties at grain boundaries clarify the nature of carrier dynamics within the 4-ABA$^+$-2D perovskite films.[28] 4-ABA$^+$ moves along the crystal boundary and recrystallize with non-reacted PbI_2, tending to cluster at the perovskite crystal boundary to crystalize as 4-ABA$^+$-2D perovskite. This process is similar to a recrystallization accompanied by grain size enlargement. The observable energy band bending at grain boundaries is supposed to promote the charge carrier separation and transport. It explains the higher V_{OC} .

The modified films exhibit lower steady-state photoluminescence (PL) peak intensity (**Figure 3d)** than the control films, suggesting that 4-ABA$^+$ can accept holes before recombination. Furthermore, the PL peak was redshifted for the 4-ABAI modified film, confirming the narrowed bandgap of the 4-ABA$^+$ modified films. Besides, the corresponding TRPL curves are recorded in **Figure 3e.** The detailed calculated PL decay constants using a bi-exponential equation are reported in **Table S2** (Supporting Information). The average decay times τ_{ave}(τ_{ave}=($A_1\tau_1^2$+ $A_2\tau_2^2$)/($A_1\tau_1$+ $A_2\tau_2$)) of the control and modified films were 578.8 ns and 273.3 ns, respectively. The TRPL result reveals that the modified perovskite film exhibits a shorter lifetime decay, indicating that the *in-situ* produced low-dimensional capping layer exhibits a better film quality, which could effectively suppress radiative recombination at the interface and promotes photogenerated charge transfer and transport ability.

J-V properties of electron-only devices with the FTO/SnO_2/perovskite/PCBM/Au structure were then employed to estimate the electron trap-state densities by the trap-filled limit voltage (V_{TFL}) measurement based on the following formula[29]:

$$V_{TEL}=\frac{L^2\, en_t}{2\varepsilon\varepsilon_0} \qquad (2)$$

where n_t is the trap-state density, e is the electron charge, L is the thickness of the perovskite layer, ε_0 is the vacuum permittivity and ε is the relative dielectric constant (~35)[30]. The V_{TFL} values of the modified and the control devices were measured at 0.11 V and 0.14 V (**Figure 3f**), respectively,

Pease cite this paper as : B. Zhang, D. Gao, M. Li, X. Shang, Y. Li, C. Chen, Th. Pauporté, Heterojunction in-situ constructed by a novel amino acid-based organic spacer for efficient and stable perovskite solar cells. ACS Appl. Mater. Interfaces, 14 (2022) 40902–40912. DOI : 10.1021/acsami.2c09926

revealing the lower trap density n_t of 1.70×10^{15} cm^{-3} for the modified device compared to 2.16×10^{15} cm^{-3} for the control one.

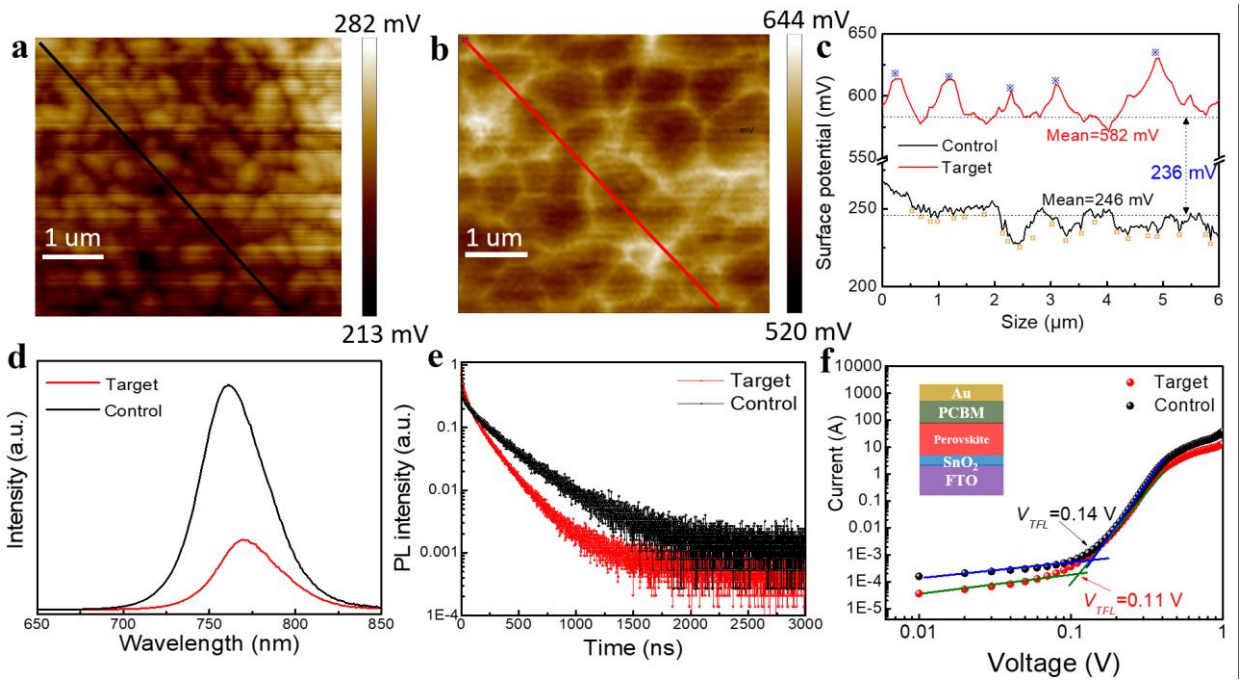

Figure 3. KPFM image of (a) control and (b) 4-ABA$^+$ modified perovskite films. (c) CPD cut lines drawn in (a) and (b). (d) Steady-state PL curves of the perovskite films deposited on glass/FTO/SnO_2 as the substrate. (e) Time-resolved PL curves of the perovskite films deposited on glass/FTO/SnO_2 as substrate. (f) *J-V* curves of the electron-only devices with the structure of FTO/SnO_2/perovskite/PCBM/Au in the dark.

DFT simulations were performed to investigate the mechanism of 4-ABA$^+$ based low-dimensional surface contact enhanced transfer of interfacial charge carriers. To simplify the structure, we constructed periodic slabs of $FAPbI_3$ and $(4\text{-ABA})_2PbI_4$ perovskite. We subsequently relaxed the position of the atoms and employed the Perdew-Burke-Ernzerhof function to get the 2D/3D structure.[31] The valence and conduction bands were mainly composed of I and Pb orbital contributions, respectively (**Figure 4a-c**). The charge carriers can be transported by the 2D/3D interface unquenched. It can be attributed to the presence of Pb-I-like bonds in both systems. The difference in charge density is also plotted to provide further insight into the mechanism of interfacial charge transport. The positive charge (yellow area) is mainly situated at the interface, close to the 3D plate. On the other hand, the negative charge (blue area) is spread near the 2D plate, which intimates that it has charge reassign between surface I of perovskite and –COOH of 4-ABA$^+$. It suggests a potent interaction between I and -COOH. This impedes the motion of I and the formation of I vacancies. It also honor forceful interplay between FA of perovskite and -COOH of 4-ABA$^+$, which curbs FA escape. The apparent distinction of negative and positive charges states that the direction of hole transport at the 2D/3D interface is directed from 3D perovskite to $(4\text{-ABA})_2PbI_4$. Therefore, the self-grown 4-ABA$^+$-2D perovskite can contribute to the hole extraction from the perovskite to the gold back electrode, thereby limiting the charge carriers recombination. To decode the influence of passivation by 4-ABA$^+$ of the perovskite

absorber, we modelled the density of partial states (PDOS) of perovskite films and 4-ABA$^+$-altered perovskite films (**Figure 4d-f**). FA vacancies, I-vacancies, and I interstitial at the perovskite surface induce trap states (highlighted by gray boxes), at the origin of non-radiative recombinations resulting in energy losses. DFT results show that 4-ABA$^+$ passivation suppresses these trap states, in agreement with the non-radiative recombination reduction determined by the TRPL results.

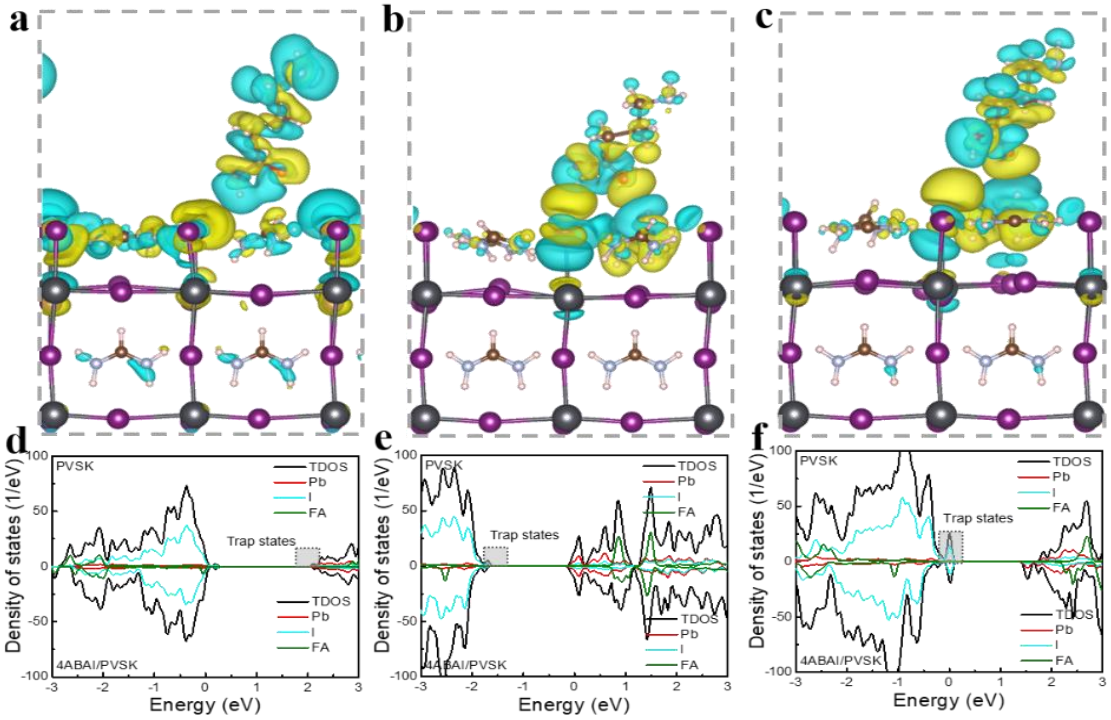

Figure 4. Charge density difference of 4-ABA$^+$ passivated perovskite surface with (a) FA-vacancy, (b) I-vacancy and (c) I-interstitial. (b) tDOS of 4-ABA$^+$ passivated perovskite surface with (d) FA-vacancy, (e) I-vacancy and (f) I-interstitial.

In addition to high efficiency, long-term stability is another key feature of PSC applications. We documented SEMs and pictures of unencapsulated $Cs_{0.05}(FA_{0.83}MA_{0.17})_{0.95}PbI_{0.83}Br_{0.17}$ perovskite films placed under high relative humidity (80±10%) stress testing. Images in **Figure 5a-b** and **S13** (Supporting Information) show that the control films were heavily decomposed with significant crystal structure degradation and pinhole formation. On the other hand, the modified films maintained an intact and flat morphology. Compared with the control perovskite films with degraded yellow color, 4-ABA$^+$ modified films exhibited no visible color change after a 25 days long storage. Therefore, the film treatment by 4-ABA$^+$ significantly enhances the ambient stability. The XRD patterns of these films (**Figure 5c-d)** confirmed that the control film decomposed markedly, with a significant increase in the PbI_2 peak intensity due to its unstable surface. On the other hand, 4-ABA$^+$ modified films exhibited no apparent XRD pattern change. The increased contact angle from 48.6° to 70.6° (**Figure 5e-f)** shows a higher hydrophobicity of the 4-ABA$^+$ modified sample. The insolubility of organic components on the top of the perovskite prevents moisture entrance into the crystal lattice. The enlarged water contact angle may be assigned to the hydrophobic alkyl chain and to the carboxyl-

carboxyl interaction of 4-ABA$^+$ in the 2D perovskite which protects water from entering into the perovskite lattice and then effectively enhances moisture stability.

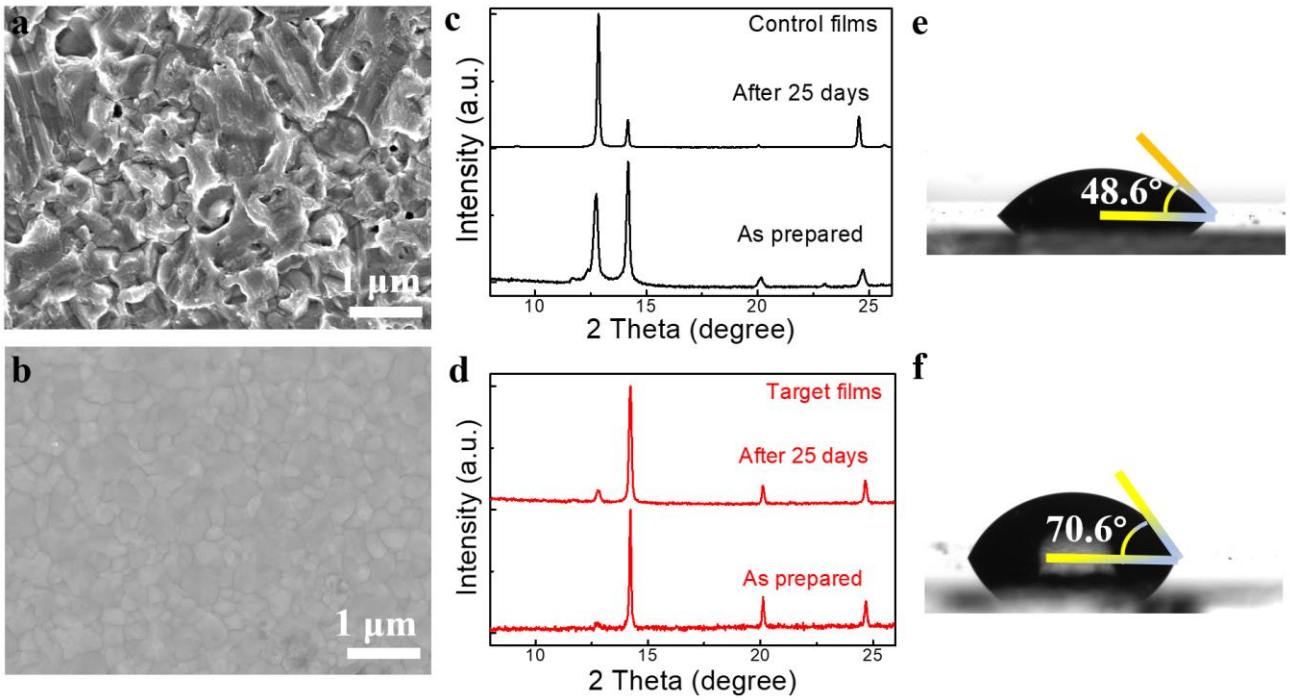

Figure 5. (a) and (b) SEM images of perovskite films stored in high humidity conditions (80±10% RH) for 25 days. (c) and (d) XRD patterns of perovskite layer before and after storage in high humidity (80±10% RH) for 25 days. (e) and (f) Water contact-angle measured on a (e) control and a (f) 4-ABA$^+$ modified perovskite films.

We monitored the photostability of the control and 4-ABA$^+$ modified $Cs_{0.05}(FA_{0.83}MA_{0.17})_{0.95}PbI_{0.83}Br_{0.17}$ devices under ageing conditions according to International Summit on Organic Photovoltaic Stability (ISOS) protocols. Precisely, the light soaking test is in line with ISOS-L-1 test regulations (**Figure 6**).[47] All the unencapsulated devices were tested in N_2 atmosphere, at room temperature, under an LED light source with an intensity of about 100 mW cm^{-2}. As a result, the control PSCs almost completely degraded from 19% to 12% within 100 h, while the 4-ABA$^+$ modified device could retain over 96% of its initial efficiency after 200 h. In particular, the control PSCs change seriously after about 80 h, which may be mainly due to the internal defects of the device and the irreversible degradation induced by ion migration. The excellent photostability of the 4-ABA$^+$ modified device in 200 h further shows that the low dimensional interfacial heterojunction can effectively passivate defects. As expected, the observed higher humidity resistance and light soaking stability of the 4-ABA$^+$ modified device results from the formation of the low-dimensional capping layer, endowing a promising practical application prospect.

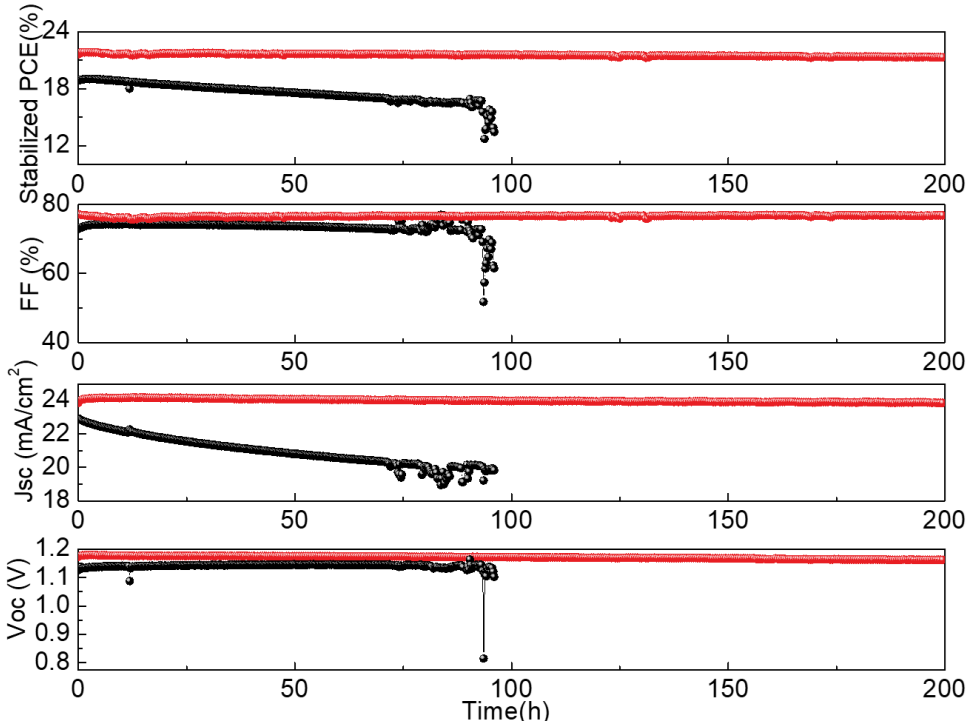

Figure 6. Light stability tracking in N_2 atmosphere to extract the photovoltaic parameters of PCE, FF, *J*sc and V_{OC} as a function of time for the unencapsulated control and 4-ABA$^+$ modified PSCs.

3. Conclusions

In conclusion, we have demonstrated a high interest in fabricating 2D/3D perovskite heterojunction structures in-situ by employing a novel multifunctional amino acid-based organic cation, 4-ABA$^+$. 4-ABA$^+$ acts as an effective interface and grain boundary passivation organic agent, which improves crystallinity, eliminates interfacial defects, and therefore reduces non-radiative recombination. The PCE was significantly enhanced from 19.86% to 23.16%, with a high V_{OC} value of 1.20 V. We have also shown that the 4-ABA$^+$ based 2D perovskite prevents moisture from entering into the perovskite lattice and improves moisture and light ageing stability over 200 h. This novel hierarchical interface perovskite fabrication method is up-and-coming for releasing highly efficient and ambient-air-stable PSCs and could assist the commercial application in the perovskite-based photovoltaic field.

4 Experimental section

4.1 DFT simulation

All first-principles calculations were based on the plane-wave pseudopotential method within the framework of density functional theory (DFT) as implemented in the Vienna Ab initio Simulation Package (VASP) with projector augmented wave (PAW) method[1-3]. For 2D perovskite and perovskite surface with 4-ABA$^+$ passivation, we used a plane-wave basis cutoff energy of 400 eV, 400 eV and 4 × 4 × 1, 2× 2 × 1 Monkhorst–Pack k-point mesh for electronic Brillouin zone integration, respectively. For the perovskite surface, we use 2× 2 × 2 supercells and a vacuum space of 15 Å for DFT. All structures were relaxed until the structures were fully optimized via total energy minimization, with

the total energy converged to less than 0.0001 eV.

4.2 Materials

CsI, PbI_2, $PbCl_2$ and $PbBr_2$ were purchased from Xi'an Polymer Light Technology Corp. FAI, MAI, MACl, MABr, 3-APAI, 4-ABAI, 5-AVAI were purchased from Greatcell Solar Limited. Dimethylsulfoxide (DMSO), *N,N*-Dimethylformaldehyde (DMF), and isopropanol (IPA) were purchased from Macklin Inc. SnO_2 was obtained from Alfa Aesar. FTO glass, [6,6]-phenyl-C61-butyric acid methyl ester (PCBM) and spiro-OMeTAD were purchased from Liaoning YouXuan Technology Co., Ltd. All these chemicals were used without further purification.

4.3 Device Fabrication.

The FTO glass substrates (TSG, 7Ω) were cleaned in a glass cleaner solution, in deionized water, and in ethanol for 20 min, in an ultrasonic bath. They were then treated by ultraviolet UV/Ozone for 5 minutes to improve the surface wettability. Next, the SnO_2 electron transporting layer was deposited by spin-coating. A droplet of SnO_2 precursor solution (2.67%, in water) was deposited onto FTO substrates, spin-coated at 3000 rpm for 30 s and annealed on a hot plate at 150 °C for 30 min.

The $Cs_{0.05}(FA_{0.83}MA_{0.17})_{0.95}PbI_{0.83}Br_{0.17}$ precursor solution was prepared by dissolving 0.172g of formamidinium iodide (FAI), 0.0224g of methylammonium bromide (MABr), 0.507g of PbI_2, and 0.0734g of $PbBr_2$ in 1 mL of DMF and DMSO (volume ratio 4:1) solvent mixture. Then, 0.320g of CsI was pre-dissolved to 1 mL DMSO. After that, 50 μL of CsI solution was added to the previous perovskite solution. The synthesized $Cs_{0.05}(FA_{0.83}MA_{0.17})_{0.95}PbI_{0.83}Br_{0.17}$ precursor solution was spin-coated onto the FTO/SnO_2 substrate at 600 rpm for 5 s and 4000 rpm for 30 s in a N_2 filled glovebox. 15s before the end of the spinning routine, 400 μL of chlorobenzene anti-solvent was dripped on the sample. The obtained film was annealed at 110°C for 60 minutes. After that, 50 μL of IPA solution containing different concentrations of 4-ABA^+ was dripped onto $Cs_{0.05}(FA_{0.83}MA_{0.17})_{0.95}PbI_{0.83}Br_{0.17}$ film (at 3000 rpm) and then sintered at 100°C for 10 min to get an optimized perovskite layer. For the CsFA perovskite precursor solution, the 1.55 M CsFA perovskite precursor was prepared for dissolving 248.16 mg of FAI, 19.73 mg of CsI, 682.13 mg of PbI_2 in a mixture of 1 mL of DMF and DMSO (4:1, v/v). Then 6.58 mg of RbI， 35 mg of MACl, 12.74 mg of $PbCl_2$, and 8.53 mg of $PbBr_2$ were added to the above precursor solution as the intermediate additives to stabilize the black phase of perovskite. The 1.55 M CsFA perovskite precursor solution was spin-coated on the FTO/SnO_2 substrate for 40 s at 4000 rpm, and then 400 μL of chlorobenzene was dropped onto the perovskite surface 15s before the program ended, and the films were annealed at 110°C for 20 min. After that, 50 μL of IPA solution containing different concentrations of 4-ABA^+ was dripped onto $Cs_{0.05}FA_{0.95}PbI_3$ film (at 3000 rpm) and then sintered at 100°C for 10 min to get an optimized perovskite layer.

We prepared a spiro-MeOTAD based hole-transporting materials solution by mixing 100 mg of spiro-MeOTAD powder, 45μL of 4-tert-butylpyridine, and 45μL of a lithium bis-(trifluoromethylsulfonyl) imide solution (340 mg/mL in acetonitrile) in 2 mL of chlorobenzene. 40 μL was deposited onto the surface of the perovskite layer and spin-coated at 3000 rpm for 30 s. Finally, a 100 nm thick Au electrode was deposited by thermal evaporation. The final device structure was FTO/SnO_2/Perovskite/Spiro-MeOTAD/Au device. A FTO/SnO_2/Perovskite/PCBM/Au structured

device was realized to estimate the electron trap-state densities. 10 mg of PCBM was dissolved in 1 mL of chlorobenzene. 50 μL of this solution was spin-coated onto the perovskite layer at 1000 rpm for 30 s and sintered at 100 °C for 30 min. The preparation method for the other layers was the same as mentioned above.

4.4 Device Characterization.

A JEOF 7610F emission scanning electron microscope (SEM) was employed to get the surface and cross-sectional morphology views of the perovskite films. X-ray diffraction (XRD) patterns for perovskite films were recorded on a Rigaku SmartLab(9Kw)DX-ray diffractometer, using a monochromatized Cu K_α target radiation source at a scanning rate of 8°/min. The scanning voltage is 5.5 kV. Agilent 5500 scanning probe microscopy was utilized for AFM topography and KPFM in tapping mode, whereas CS-AFMin contact mode with 1 V applied bias. Impedance spectra were measured with a Electrochemical Workstation (AMETEK, VersaSTAT3) and the data were processed using Z-View program. The absorption spectra were measured by a Shimadzu UV-1900 spectrometer. TRPL and steady-state PL spectra were acquired by employing the FLS980 Series of Fluorescence Spectrometers with an excitation wavelength of 480 nm. The *J-V* characteristics were measured under AM 1.5 G irradiation using a 71S type solar simulator system customized by SOFN Instruments Co., Ltd., coupled with a Keithley 2400 digital source meter. A reference silicon cell was used for the system calibration. ISOS-L-1 stability testing in this work stands for the light photostability at room temperature with a white LED-based solar simulator (Mato-led-90, Tianjin Meitong Corp., China.) under the open-voltage condition. The LED light source contains wavelength ranges from 400 to 950 nm with a calibrated irradiation intensity of 100±2 $mW.cm^{-2}$. The ageing test electrical data was acquired using the Keithley 2400 source meter controlled by the software (designed for Keithley 2400 fully automatic control) developed by Wuhan Zeal Young Technology Co., Ltd. The self-made ageing test instrument for light photostability regularly scans the *J-V* curve to obtain the total data of photovoltaic parameters (PCE, *V*oc, *J*sc and FF) changing with ageing time. The unencapsulated solar cell devices were placed in pure N_2 (>99.99%) atmosphere with a chamber temperature kept at 25 ± 3 °C.

Except for special emphasis (such as the *J-V* curve of champion devices), most of the figures mentioned are obtained from the three cation $Cs_{0.05}(FA_{0.83}MA_{0.17})_{0.95}PbI_{0.83}Br_{0.17}$ precursor-based perovskite films. This is mainly because the CsFA perovskite with higher FA ratio exhibit low bandgap and relatively high efficiency, while its environmental humidity stability is relatively poor, and it is easy to change from black α-phase to yellow δ-phase in the air environment, which affects the analysis of 4-ABA^+ function on the perovskite. In contrast, the three cation $Cs_{0.05}(FA_{0.83}MA_{0.17})_{0.95}PbI_{0.83}Br_{0.17}$ exhibit overall better Operation and storage stability for characterization and analysis.

Acknowledgments

This work was supported by the National Natural Science Foundation of China (Grant Nos. 62004058, U21A2076, 52071048), Nature Science Foundation of Hebei Province (F2020202022), the

Open Fund of the State Key Laboratory of Integrated Optoelectronics (IOSKL2020KF09), State Key Laboratory of Reliability and Intelligence of Electrical Equipment (No. EERI_PI20200005, EERI_0Y2021001), The Central Guidance on Local Science and Technology Development Fund of Hebei Province(Grant No. 226Z4305G).

Supporting Information

Grain size distribution histograms of the 3D perovskite film; XPS survey spectra of the perovskite films; FTIR spectra of perovskite film; XRD patterns of 4-ABA^+ 2D perovskite phase; UV-Vis spectra of perovskite films; DFT calculations of $(BA)_2MAPb_2I_7$, $(4\text{-}ABA)_2MAPb_2I_7$, and $(5AVA)_2MAPb_2I_7$ structures; Statistical analysis of the effect of 4-ABAI concentration on the V_{OC}, FF, and J_{SC} solar cell parameters; EQE spectra; Stabilized output of the cells; Dark *J-V* curves of PSCs; *J-V* curves of solar cells with and without 4-ABA^+; *J-V* curves of cells treated with 3-APA^+ and 5-AVA^+; Photographs of perovskite films stored in high humidity conditions; Table of structural data of the optimized $BA)_2MAPb_2I_7$ and $(4\text{-}ABA)_2MAPb_2I_7$ structure; Table of average TRPL curve analysis parameters.

Author contributions

C.C supervised the project. C.C. B.B. and T.P. conceived and designed the experiments. B.Z and Y.L developed the DFT calculations. G.D. performed the EQE experiments. M.L., B.Z., and X.S., conducted optical absorption and fluorescence measurements and prepared all samples. X.S performed the SEM and KPFM measurements. B.Z., C.C., and T.P. wrote the manuscript with input from all authors. All authors have given approval to the final version of the manuscript.

Competing interests

The authors declare no competing interests.

References

1. Zhao, Y.; Ma, F.; Qu, Z.H.; Yu, S.Q.; Shen, T.; Deng, H.X.; Chu, X.B.; Peng, X.X.; Yuan, Y.B.; Zhang, X.W.; You, J.B.; Inactive $(PbI_2)_2RbCl$ Stabilizes Perovskite Films for Efficient Solar Cells. *Science* **2022**, *377*, 531-534.

2. Li, M.; Li, H.; Zhuang, Q.; He, D.; Liu, B.; Chen, C.; Zhang, B.; Pauporté, T.; Zang, Z.; Chen, J., Stabilizing Perovskite Precursor by Synergy of Functional Groups for NiOx-Based Inverted Solar Cells with 23.5 % Efficiency. *Angew. Chem., Int. Ed.* **2022**, e202206914.

3. Chen, C.; Liu, D.; Zhang, B.; Bi, W.; Li, H.; Jin, J.; Chen, X.; Xu, L.; Song, H.; Dai, Q., Carrier Interfacial Engineering by Bismuth Modification for Efficient and Thermoresistant Perovskite Solar Cells. *Adv. Energy. Mater.* **2018**, *8*, 201703659.

4. Tan, H.R.; Jain, A.; Voznyy, O.; Lan, X.Z.; de Arquer, F.P.G.; Fan, J.Z.; Quintero-Bermudez, R.; Yuan, M.J.; Zhang, B.; Zhao, Y.C.; Fan, F.J.; Li, P.C.; Quan, L.N.; Zhao, Y.B.; Lu, Z.H.; Yang, Z.Y.; Hoogland, S.; Sargent, E.H.; Efficient and Stable Solution-Processed Planar Perovskite Solar Cells Via Contact Passivation. *Science* **2017**, 355, 722-726.

5. Gao, D.Y.; Yang, L.Q.; Ma, X.H.; Shang, X.N.; Wang, C.; Li, M.J.; Zhuang, X.M.; Zhang, B.X.; Song, H.W.; Chen, J.Z.;

Chen, C.; Passivating Buried Interface with Multifunctional Novel Ionic Liquid Containing Simultaneously Fluorinated Anion and Cation Yielding Stable Perovskite Solar Cells over 23% Efficiency. *J. of Energy Chem.* **2022**, *69*, 659-666.

6. Yao, D.; Zhang, C.; Zhang, S.; Yang, Y.; Du, A.; Waclawik, E.; Yu, X.; Wilson, G. J.; Wang, H., 2D–3D Mixed Organic–Inorganic Perovskite Layers for Solar Cells with Enhanced Efficiency and Stability Induced by N-Propylammonium Iodide Additives. *ACS Appl. Mater. Interfaces* **2019**, *11*, 29753-29764.

7. Hu, J.L.; Wang, C.; Qiu, S.D.; Zhao, Y.C.; Gu, E.; Zeng, L.X.; Yang, Y.Z.; Li, C.H.; Liu, X.H.; Forberich, K.; Brabec, C.J.; Nazeeruddin, M.K.; Mai, Y.H.; Guo, F, Spontaneously Self-Assembly of a 2D/3D Heterostructure Enhances the Efficiency and Stability in Printed Perovskite Solar Cells. *Adv. Energy Mater.* **2020**, *10*, 2000173.

8. Ngo, T. T.; Suarez, I.; Antonicelli, G.; Cortizo-Lacalle, D.; Martinez-Pastor, J. P.; Mateo-Alonso, A.; Mora-Sero, I., Enhancement of the Performance of Perovskite Solar Cells, Leds, and Optical Amplifiers by Anti-Solvent Additive Deposition. *Adv. Mater.* **2017**, *29*, 1604056.

9. D. Zheng, D.; T. Zhu, T.; Y. Yan, Y.; Th. Pauporté, T.; Controlling the formation process of methylammonium-free halide perovskite films for a homogeneous incorporation of alkali metal cations beneficial to solar cell performances. A*dv. Energy Mater*. **2022**, *12*, 2103618.

10. Zhu, L.; Zhang, X.; Li, M.; Shang, X.; Lei, K.; Zhang, B.; Chen, C.; Zheng, S.; Song, H.; Chen, J., Trap State Passivation by Rational Ligand Molecule Engineering toward Efficient and Stable Perovskite Solar Cells Exceeding 23% Efficiency. *Adv. Energy Mater.* **2021**, *11*, 2100529.

11. Bush, K. A.; Cheacharoen, R.; Beal, R.; Bowring, A. R.; McGehee, M. D., Towards Enabling Stable Lead Halide Perovskite Solar Cells; Interplay between Structural, Environmental, and Thermal Stability. *J. Mater. Chem. A* **2017**.

12. Kim, B.; Seok, S. I., Molecular Aspects of Organic Cations Affecting the Humidity Stability of Perovskites. *Energy Environ. Sci.* **2020**, *13*, 805-820.

13. Zhu, T.; Zheng, D.; Liu, J.; Coolen, L.; Pauporté, T. PEAI-Based Interfacial Layer for High-Efficiency and Stable Solar Cells Based on a MACl-Mediated Grown $FA_{0.94}MA_{0.06}PbI_3$ Perovskite. *ACS Appl. Mater. Interfaces* **2020**, *12*, 37197−37207

14. (a) Sheng, Y.; Mei, A.; Liu, S.; Duan, M.; Jiang, P.; Tian, C.; Xiong, Y.; Rong, Y.; Han, H.; Hu, Y., Mixed (5-Ava)Xma1−Xpbi3−Y(Bf4)Y Perovskites Enhance the Photovoltaic Performance of Hole-Conductor-Free Printable Mesoscopic Solar Cells. *J. Mater. Chem. A* **2018**, *6*, 2360-2364. (b) Liu, Y., et al., Ultrahydrophobic 3D/2D Fluoroarene Bilayer-Based Water-Resistant Perovskite Solar Cells with Efficiencies Exceeding 22%. *Sci. Adv.* **2019**, *5*, eaaw2543.

15. Zheng, D.; Tong, C.; Zhu, T.; Rong, Y.; Pauporté, T., Effects of 5-Ammonium Valeric Acid Iodide as Additive on Methyl Ammonium Lead Iodide Perovskite Solar Cells. *Nanomaterials (Basel)* **2020**, *10,* 2512.

16. Mei, A.Y.; Sheng, Y.S.; Ming, Y.; Hu, Y.; Rong, Y.G.; Zhang, W.H.; Luo, S.L.; Na, G.R.; Tian, C.B.; Hou, X.M.; Xiong, Y.L.; Liu, S.; Uchida, S.; Kim, T.W..; Yuan, Y.B.; Zhang, L.J.; Zhou, Y.H.; Han, H.W.; Stabilizing Perovskite Solar Cells to IEC61215:2016 Standards with over 9,000-H Operational Tracking. *Joule* **2020,** *4*, 2646-2660.

17. Zhang, Q.; Zhao, J.; Xiao, Z.; Zhou, J.; Hong, B.; Luo, Z.; Bao, J.; Gao, C., Improved Moisture Stability of 2D Hybrid Perovskite $(HOOC–CH_2–NH_3)_2PbI_4$ by Dehydration Condensation between Organic Components. *ACS Appl. Energy Mater.* **2018**, *1*, 2502-2511.

18. Jiang, Q.; Chu, Z.; Wang, P.; Yang, X.; Liu, H.; Wang, Y.; Yin, Z.; Wu, J.; Zhang, X.; You, J., Planar-Structure Perovskite Solar Cells with Efficiency Beyond 21 %. *Adv. Mater.* **2017**, *29*.

19. Duong, T.; Wu, Y.L.; Shen, H.P.; Peng, J.; Fu, X.; Jacobs, D.; Wang, E.C.; Kho, T.C.; Fong, K.C.; Stocks, M.; Franklin, E.; Blakers, A.; Zin, N.; McIntosh, K.; Li, W.; Cheng, Y.B.; White, T.P.; Weber, K.; Catchpole, K.; Rubidium Multication Perovskite with Optimized Bandgap for Perovskite-Silicon Tandem with over 26% Efficiency. *Adv. Energy Mater.* **2017**, *7*, 1700228.

20. Yang, Y.Q.; Wu, J.H.; Wang, X.B.; Guo, Q.Y.; Liu, X.P.; Sun, W.H.; Wei, Y.L.; Huang, Y.F.; Lan, Z.; Huang, M.L.; Lin, J.M.; Chen, H.W.; Wei, Z.H.; Suppressing Vacancy Defects and Grain Boundaries Via Ostwald Ripening for High-Performance and Stable Perovskite Solar Cells. *Adv Mater* **2020**, *32*, e1904347.

21. Shi, E.; Gao, Y.; Finkenauer, B. P.; Akriti; Coffey, A. H.; Dou, L., Two-Dimensional Halide Perovskite Nanomaterials and Heterostructures. *Chem. Soc. Rev.* **2018**, *47*, 6046-6072.

22. Tsai, H.H.; Nie, W.Y.; Blancon, J.C.; Toumpos, C.C.S.; Asadpour, R.; Harutyunyan, B.; Neukirch, A.J.; Verduzco, R.; Crochet, J.J.; Tretiak, S.; Pedesseau, L.; Even, J.; Alam, M.A.; Gupta, G.; Lou, J.; Ajayan, P.M.; Bedzyk, M.J.; Kanatzidis, M.G. ; Mohite, A.D.; High-Efficiency Two-Dimensional Ruddlesden–Popper Perovskite Solar Cells. *Nature* **2016**, *536*, 312-316.

23. Grancini, G.; Nazeeruddin, M. K., Dimensional Tailoring of Hybrid Perovskites for Photovoltaics. *Nature Rev. Mater.* **2019**, *4*, 4-22.

24. Ye, J. Y.; Tong, J.; Hu, J.; Xiao, C.; Lu, H.; Dunfield,S.P.; Kim, D.H.; Chen, X.; Larson, B.W.; Hao, J.; Wang, K.; Zhao, Q.; Chen, Z.; Hu, H.; You, W.; Berry, J.J.; Zhang, Zhu K., Enhancing Charge Transport of 2D Perovskite Passivation Agent for Wide-Bandgap Perovskite Solar Cells Beyond 21%. *Solar RRL* **2020**, *4*, 2000082.

25. Zheng, D.; Zhu, T.; Pauporté, T. A Co-Additives Strategy for Blocking Ionic Mobility in Methylammonium-Free Perovskite Solar Cells and High Stability Achievement. Solar RRL., **2021**, *5*, 2100010.

26. (a) Zhou, T.; Lai, H.; Liu, T.; Lu, D.; Wan, X.; Zhang, X.; Liu, Y.; Chen, Y., Highly Efficient and Stable Solar Cells Based on Crystalline Oriented 2D/3D Hybrid Perovskite. *Adv. Mater.* **2019**, *31*, 1901242. (b) Chen, Y.; Sun, Y.; Peng, J.; Zhang, W.; Su, X.; Zheng, K.; Pullerits, T.; Liang, Z., Tailoring Organic Cation of 2D Air-Stable Organometal Halide Perovskites for Highly Efficient Planar Solar Cells. *Adv. Energy Mater.*, **2017**, *20*, 1700162.

27. Wang, Y.; Hu, Z.; Gao, C.; Yang, C.; Zhang, J.; Zhu, Y., Comprehensive Elucidation of Grain Boundary Behavior in All‐Inorganic Halide Perovskites by Scanning Probe Microscopy. *Adv. Mater. Interfaces* **2020**, *7*, 1901521.

28. Chen, Q.; Zhou, H.P.; Fang, Y.H.; Stieg, A.Z.; Song, T.B.; Wang, H.H.; Xu, X.B.; Liu, Y.S.; Lu, S.R.; You, J.B.; Sun, P.Y.; Mckay, J.; Goorsky, M.S.; Yang, Y.; The Optoelectronic Role of Chlorine in CH3NH3PbI3(Cl)-Based Perovskite Solar Cells. *Nature Commun.* **2015**, *6*, 7269.

29. Liu, Y.C.; Zhang, Y.X.; Zhu, X.J.; Yang, Z.; Ke, W.J.; Feng, J.S.; Ren, X.D.; Zhao, K.; Liu, M.; Kanatzidis, M.G.; Liu, S.Z.; Inch-Sized High-Quality Perovskite Single Crystals by Suppressing Phase Segregation for Light-Powered Integrated Circuits. *Sci. Adv.* **2021**, *7*, eabc8844.

30. Lin, Q.; Armin, A.; Nagiri, R. C. R.; Burn, P. L.; Meredith, P., Electro-Optics of Perovskite Solar Cells. *Nat. Photonics* **2014**, *9*, 106-112.

31. Zheng, Y.; Yang, X.; Su, R.; Wu, P.; Gong, Q.; Zhu, R., High-Performance $CsPbI_xBr_{3-x}$ All-Inorganic Perovskite Solar Cells with Efficiency over 18% Via Spontaneous Interfacial Manipulation. *Adv. Funct. Mater.* **2020**, *30*, 2000457.

Pease cite this paper as : B. Zhang, D. Gao, M. Li, X. Shang, Y. Li, C. Chen, Th. Pauporté, Heterojunction in-situ constructed by a novel amino acid-based organic spacer for efficient and stable perovskite solar cells. ACS Appl. Mater. Interfaces, 14 (2022) 40902–40912. DOI : 10.1021/acsami.2c09926

Table of Content